Quantum Emitter Formation Dynamics and Probing of Radiation-Induced Atomic Disorder in Silicon

Wei Liu,[1,*,†] Vsevolod Ivanov,[1,2,†] Kaushalya Jhuria,[1] Qing Ji,[1] Arun Persaud,[1] Walid Redjem,[3] Jacopo Simoni,[2] Yertay Zhiyenbayev,[3] Boubacar Kante,[3] Javier Garcia Lopez,[4] Liang Z. Tan,[2] and Thomas Schenkel[1]

[1] *Accelerator Technology and Applied Physics Division, Lawrence Berkeley National Laboratory, Berkeley, California 94720, USA*

[2] *Molecular Foundry, Lawrence Berkeley National Laboratory, Berkeley, California 94720, USA*

[3] *Department of Electrical Engineering and Computer Sciences, University of California, Berkeley, California 94720, USA*

[4] *Centro Nacional de Aceleradores, Universidad de Sevilla, Consejo Superior de Investigaciones Científicas (CSIC), Junta de Andalucia, Seville 41092, Spain*

(Received 13 March 2023; revised 21 March 2023; accepted 22 June 2023; published 26 July 2023)

Near-infrared color centers in silicon are emerging candidates for on-chip integrated quantum emitters, optical-access quantum memories, and sensing. We access ensemble G-color-center formation dynamics and radiation-induced atomic disorder in silicon for a series of megaelectronvolt proton-flux conditions. The photoluminescence results reveal that the G centers are formed more efficiently by pulsed-proton irradiation than by continuous-wave proton irradiation. The enhanced transient excitations and dynamic annealing within nanoseconds allows optimization of the ratio of G-center formation to nonradiative defect accumulation. The G centers preserve narrow line widths of about 0.1 nm when they are generated by moderate pulsed-proton fluences, while the line width broadens significantly as the pulsed-proton fluence increases. This implies vacancy or interstitial clustering by overlapping collision cascades. The tracking of G-center properties for a series of irradiation conditions enables sensitive probing of atomic disorder, serving as a complementary analytical method for sensing damage accumulation. Aided by *ab initio* electronic structure calculations, we provide insight into the atomic disorder induced inhomogeneous broadening by introducing vacancies, silicon interstitials, and oriented strain fields in the vicinity of a G center. A vacancy leads to a tensile strain and can result in either a red shift or a blue shift of the G-center emission, depending on its position relative to the G center. Meanwhile, Si interstitials lead to compressive strain, which results in a monotonic red shift. High-flux and tunable ion pulses enable the exploration of the fundamental dynamics of radiation-induced defects as well as methods for the optimization of G-center formation and qubit synthesis for quantum information processing.

DOI: 10.1103/PhysRevApplied.20.014058

I. INTRODUCTION

Programmable quantum information processing and unbreakable secure quantum networks linked by trusted repeater nodes require the robust generation and manipulation of single and a few quanta in a scalable platform with long coherence times [1–3]. On-chip integrated quantum photonic circuits in silicon (Si) have been used to demonstrate the implementation of quantum protocols via multiplexed linear optical elements and nonlinear electro-optic effects, due to its mature manufacturing and low optical losses [4,5]. However, because of the indirect band gap of silicon, it has been a long-standing challenge to fabricate highly efficient silicon-based quantum emitters enabling on-demand single photons, entangled-photon pairs, spin-photon entanglements, squeezed light, etc. Although the integration of heterogeneous active sources has been implemented using [6], e.g., III-V quantum dots, color centers in diamond or SiC, and spontaneous parametric down-conversion (SPDC) nonlinear materials, searching for emissive qubits in silicon as a host material [7] is desirable for CMOS-process compatibility and scaling-up purposes. Alternatively, the direct formation of telecom-band light-emitting defects in silicon through the nonionizing energy loss (NIEL) of energetic particles has become an emerging approach for on-chip integration, as recently demonstrated using carbon-based defect complexes of G and T centers [8–13], as well as rare-earth

*weiliu01@lbl.gov

†These authors contributed equally.

erbium ions [14,15]. On the other hand, it is well known that irradiating a semiconductor with energetic particles gives rise to structural damage and defect formation via NIEL processes [16]. This leads to degradation of the device performance, e.g., in radiation detectors operating in (high-)radiation environments. Radiation-damage effects include reduced sensitivity of photodiodes [17], decreased efficiency of light-emitting diodes (LEDs), and lasing threshold shifts [18], as well as degradation of the reliability of power electronics [19]. The build-up of stable radiation damage often proceeds via complex dynamic annealing (DA) processes, involving point-defect migration and interaction, which often occurs during the ion-implantation or -irradiation step for actual device fabrication and depends on the density of collision cascades and the ion-beam flux [20,21]. Such dose-rate effects on the radiation-damage and defect-interaction dynamics in silicon have been studied by various analytical methods, including deep-level transient spectroscopy (DLTS) [22,23], charge-collection efficiency (CCE) measurements [24], Rutherford back-scattering spectroscopy (RBS) [25, 26], x-ray diffraction analysis (XRD), and positron-annihilation Doppler-broadening spectroscopy (PAS) [27]. However, the effect of the ion dose rate on the formation dynamics of color centers and the correlation between inhomogeneous broadening and atomic radiation disorder have rarely been studied, even though understanding these processes is essential for optimizing the formation yield, coherence, luminescence efficiency, and deterministic positioning of these defect emitters in silicon quantum photonic circuits [12].

Ion implantation will likely play an essential role in future large-scale fabrication of quantum defects in silicon. The integration of large numbers of qubits requires efficient and ideally deterministic formation of quantum defects of consistently high quality in photonic devices. The development of defect-center formation techniques that minimize inhomogeneous line-width broadening due to radiation damage has remained challenging [28,29]. Here, we explore radiation-induced G-center formation dynamics in silicon wafers under various proton-irradiation conditions: (1) by using the induction linear accelerator that is part of the Neutralized Drift Compression Experiment (NDCX-II) at the Lawrence Berkeley National Laboratory, which delivers an approximately 1-MeV intense nanosecond-pulsed proton beam and allows us access to transient radiation effects on defect dynamics far from equilibrium at the nanosecond time scale [10,30]; and (2) by using 1-MeV continuous-wave (cw) proton irradiation with orders-of-magnitude-lower dose rates performed in the Centro Nacional de Aceleradores, Seville, Spain [31]. Our present study complements earlier silicon-irradiation studies with pulsed-proton and ion pulses from laser accelerators and higher damage rates [32]. We compare the G-center optical properties characterized by time-resolved photoluminescence (PL) and reveal the dose-rate effect on color-center formation efficiency and optical line width. Furthermore, we perform *ab initio* electronic structure calculations, which provide insight into the atomic disorder induced inhomogeneous broadening, by introducing vacancies, Si interstitials, and oriented strain fields in the vicinity of a G center. We highlight the approach of using pulsed-proton irradiation on the as-received carbon silicon wafers to generate color-center complexes with high formation efficiency while preserving the narrow line width. Our results can guide directions for the efficient formation of (single) G centers by pulsed single-shot ion implantation and we demonstrate this using G centers as a sensitive optical probe for atomic scale radiation-induced disorder.

II. SAMPLES AND MEASUREMENTS

Float-zone silicon with residual carbon, with a (111) crystallographic plane and an approximately 100-Ω cm resistivity, was used as the starting material for proton-beam irradiation. Note that the as-received carbon in the silicon samples is likely due to the extended storage and that no additional carbon implantation or annealing was performed in the experiments that we report here. Such a starting material circumvents the typical carbon-implantation step for G-center formation, which introduces radiation damage [33,34]. Secondary-ion mass spectrometry (SIMS) prior to irradiation showed a carbon-atom concentration of up to 10^{20} C/cm^3 near the native oxide surface, which fell to the SIMS sensitivity limit of 10^{16} C/cm^3 at a depth of 150 nm, corresponding to a carbon areal density of 2×10^{14} C/cm^2 [10].

Pulsed-proton irradiation was performed by NDCX-II, which delivers protons of up to 1.1 MeV for an approximately 10-ns pulsed length, with a repetition rate of one shot per 45 s and an energy spread of ±50 keV [35]. A 1-MeV proton generates dilute vacancies and interstitials at a rate of approximately 2×10^{-4} damage events per proton per nanometer in the top 1 μm of the samples [10]. A 4-μm-thick aluminum foil in front of the sample was used to filter out any residual low energy H_2^+ ions, which results in a 0.9-MeV proton landing on an approximately 2-mm-diameter area of the sample. Two different dose rates of $7.9 \pm 1.6 \times 10^{10}$ protons per cm^2 per pulse (transient ion flux of 7.9×10^{18} protons per cm^2 per second) and $6.9 \pm 1.6 \times 10^9$ protons per cm^2 per pulse (transient ion flux of 6.9×10^{17} protons per cm^2 per second), determined by Faraday-cup measurements on a series of pulses collected both before and after the NDCX-II, were used to irradiate the sample. On the other hand, 1-MeV cw proton irradiation with a ±2 keV energy spread was performed on the same batch of silicon wafers. For the fluences of 1×10^{11} cm^{-2} and 1×10^{12} cm^{-2}, the beam current was approximately 10 pA (ion flux of 8×10^9 protons per cm^2

per second), while for the higher fluences (1×10^{13} cm^{-2} and 1×10^{14} cm^{-2}), the beam current was approximately 1 nA (ion flux of 8×10^{11} protons per cm^2 per second). We did not anneal the silicon samples prior to the PL measurements.

PL spectra were recorded at 4 K using a confocal near-infrared micro-PL setup. Optical excitation was performed with a pulsed laser (2 MHz, 532 nm) focused onto the sample via an objective (N.A. = 0.85), which provides about 0.6-μm diameter at focus and 1-μm depth of field. The PL spectrum was collected by the same objective and guided to a spectrometer (with grating of 1200 grooves per millimeter) coupled to an InGaAs camera, which provides better than 0.03-nm spectral resolution. The time-resolved PL was measured by using a superconducting single-photon detector (SNSPD) with a band-pass filter (tunable center wavelength around 1300 nm and 12-nm bandwidth), which provides a detection efficiency of 85%.

III. EXPERIMENTAL RESULTS

A. Proton fluence and dose-rate effect on G-center formation dynamics

Figure 1(a) presents an example of the ensemble G-center PL zero-phonon line (ZPL) around 1278 nm generated by pulsed-proton irradiation of one, five, 20, and 100 shots of $7.9 \pm 1.6 \times 10^{10}$ cm^{-2} per pulse. The gradual increase of the PL intensity of G centers as the proton fluence increases up to 1.6×10^{12} cm^{-2} (for 20 shots) is evidence for the direct formation of G centers by proton-induced Si interstitials combining with carbon pairs formed by a substitutional carbon trapping a migrating carbon interstitial [33,34]. Both radiative and nonradiative recombination channels contribute to the time-integrated PL intensity, which is proportional to the internal quantum efficiency as detailed in Sec. I of the Supplemental Material [36]. The increase of the time-integrated PL with the increase of the proton fluence reveals the dominant radiative recombination by the increase of the G-center density. As the proton fluence increases to $7.9 \pm 1.6 \times 10^{12}$ cm^{-2} per pulse by 100 shots, the PL intensity drops significantly. This PL-intensity drop can be related to either an increase of the nonradiative channel by radiation damage or a reduced yield of G centers. Note that the repeated pulses can lead to annealing or may alter the vacancies or interstitials and G centers that have been formed by the preceding pulses. Here, we expect the heating effect from the energy deposition by the proton pulses to be marginal, because of only an approximately 4-K temperature variation generated by each pulsed proton at a depth of 0.5 μm in the silicon [10].

We further compare the dose-rate effect on the G-center formation dynamics. Figure 1(b) summarizes the integrated PL intensity of G centers generated by multiple pulsed-proton shots with $7.9 \pm 1.6 \times 10^{10}$ cm^{-2} per pulse (black dot), $6.9 \pm 1.6 \times 10^{9}$ cm^{-2} per pulse (red), and cw protons (blue dot), with the proton fluence varying from 10^{11} cm^{-2} to 10^{14} cm^{-2}. The scaling of the PL intensity with the proton fluence is larger for pulsed irradiation with a power-law exponent of 0.65, compared to 0.17 for the cw case. This shows that pulsed irradiation with a higher proton flux favors G-center formation.

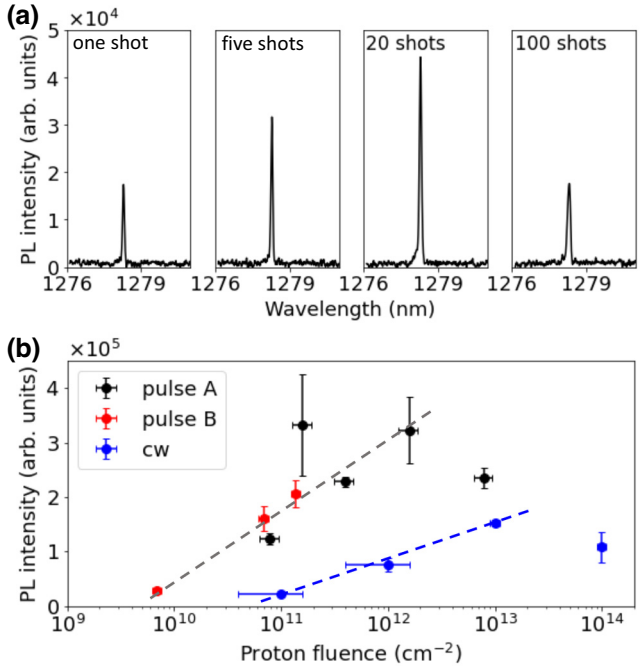

FIG. 1. (a) An example of the PL spectra of G centers created by one, five, 20, and 100 shots of $7.9 \pm 1.6 \times 10^{10}$ protons per cm^2 per pulse, respectively, with a laser pump power of 0.3 mW. (b) A comparison of the integrated PL intensity of G centers generated by $7.9 \pm 1.6 \times 10^{10}$ protons per cm^2 per pulse (labeled as pulse A, black dot), $6.9 \pm 1.6 \times 10^{9}$ protons per cm^2 per pulse (labeled as pulse B, red dot), and a cw proton (blue dot), with the proton fluence varying from 10^{11} cm^{-2} to 10^{14} cm^{-2}.

B. Carrier-recombination dynamics by time-resolved PL

We perform time-resolved PL measurements to investigate the dose-rate effect on the carrier-recombination dynamics of radiation-induced G centers. Figures 2(a) and 2(b) show the example of PL decays of G centers created by pulsed protons ($7.9 \pm 1.6 \times 10^{10}$ protons per cm^2 per pulse) by varying the number of shots from 1 to 100 and by cw proton irradiation with the fluence varying from 1×10^{11} cm^{-2} to 1×10^{14} cm^{-2}. For both pulsed and cw irradiation, the PL decay becomes faster with increasing proton fluence, which results from two aspects: the increase of the radiative rate by increasing the G-center density N_G; and the increase of the nonradiative rate due to the increase of the Shockley-Read-Hall (SRH) deep-level defect density N_{non}. As shown in Sec. II of the

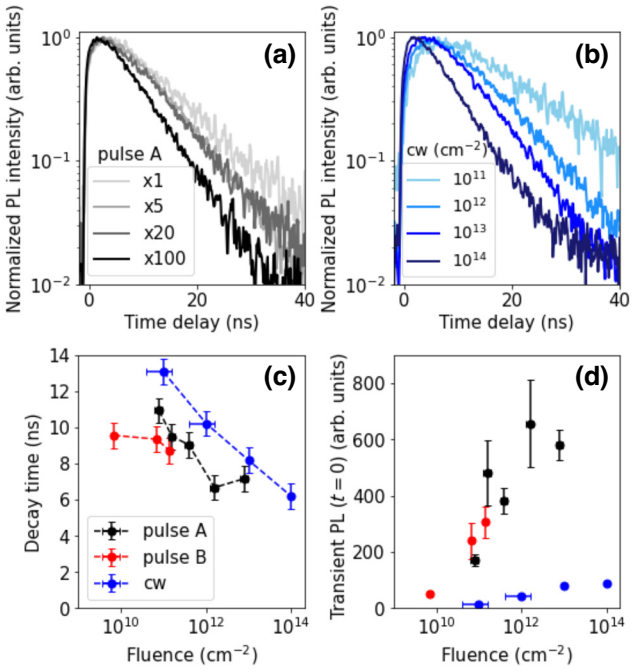

FIG. 2. (a) The time-resolved PL of G centers created by pulsed-proton ($7.9 \pm 1.6 \times 10^{10}$ protons per cm^2 per pulse) irradiation by varying the number of shots from one to 100, respectively. (b) The time-resolved PL of G centers created by cw proton irradiation with the fluence varying from 1×10^{11} cm^{-2} to 1×10^{14} cm^{-2}. (c) The effective PL decay time extracted using single-exponent fitting of the experiments as a function of the proton fluence by using a pulse of $7.9 \pm 1.6 \times 10^{10}$ protons per cm^2 per pulse (black dots), $6.9 \pm 1.6 \times 10^{9}$ protons per cm^2 per pulse (red dots), and cw proton irradiation (blue dots and dashed lines as guides to the eye). (d) The corresponding transient PL intensity at initial delay as a function of the proton fluence by using pulsed and cw proton irradiation.

Supplemental Material [36], the increase of the PL decay time with the laser pump power is consistent with the typical feature of the gradual saturation of the nonradiative SRH process, which demonstrates the presence of radiation-damage-induced nonradiative defects [34]. The nonradiative defects can be the vacancy-related deep-level states, e.g., a divacancy with 0.42 eV below the conduction band or higher-order vacancy clusters [23,37], the density of which can be further quantified by deep-level transient spectroscopy (DLTS) and electron spin resonance (ESR) [38].

Note that the radiative rate (ρ_G) for individual G centers is expected to remain constant within a relatively dilute density range (with no or only very minimal dipole-dipole coupling between G centers) and is dominated by the intrinsic dipole moment of individual G centers. Such assumptions are reasonable in our sample, in which the upper bound of the G density within 50 nm is 1×10^{12} cm^{-2}, created by the 1×10^{14} cm^{-2} proton irradiation, considering the 2×10^{-4} damage events per proton per nanometer generated by the approximately 1-MeV proton. It is worth noting that, as shown in Fig. 2(b), the rise time of the PL intensity (τ_{rise}) to its maximum is gradually delayed as the cw proton fluence decreases. This indicates a longer carrier diffusion length before capture by either G centers or by nonradiative defects, with a larger average distance in the dilute density range. As a comparison, the τ_{rise} of the G center is sharp in the case of pulsed irradiation, which can be ascribed to the fast capture of carriers by the higher amount of G-center formation or nonradiative defect density, therefore leading to a short carrier diffusion length.

Figure 2(c) summarizes the effective PL decay time of G centers extracted by single-exponent fitting of the experiments as a function of the proton fluence, using multipulses of $7.9 \pm 1.6 \times 10^{10}$ protons per cm^2 per pulse (black dots), $6.9 \pm 1.6 \times 10^{9}$ protons per cm^2 per pulse (red dots), and cw proton irradiation (blue dots). As the cw proton fluence is increased from 1×10^{11} cm^{-2} to 1×10^{14} cm^{-2}, the decay time gradually decreases from 13 ns to 6 ns. The PL lifetime of G centers formed by the pulse irradiation follows a trend similar the one for cw. Referring to the reported single isolated G-center decay time of > 45 ns [9], the shorter decay time that we observe here is composed of a radiative channel of G center and parasitic nonradiative defect channels. Assuming $\tau_r = 45$ ns, the quantum efficiency of the ensemble G centers is about 29%–13% in our case, corresponding to a nonradiative lifetime τ_{nr} of 18 ns – 7 ns. On the other hand, the approximately 6-ns decay time at 1×10^{14} cm^{-2} proton fluence is consistent with the reported G centers generated by similar proton irradiation [33], which suggests a characteristic decay time dominated by the nonradiative defects induced by the elevated radiation damage.

Figure 2(d) compares the corresponding transient PL intensity of G centers at initial delay as a function of the proton fluence by using pulsed and cw proton irradiation. Importantly, the transient PL intensity at initial delay can be safely assumed to be proportional to the G-center density N_G (namely, $\propto \sigma_G \rho_G N_G$, where σ_G is the capture cross section of the individual G center), if the τ_{nr} is orders of magnitude larger than the time resolution [39,40], a condition that is fulfilled in our study considering the nanosecond range of τ_{nr} compared to the 100-ps resolution of our setup. As presented in Fig. 2(d), the scaling of the transient PL intensity ($\propto N_G$) to the proton fluence is much larger for the pulsed irradiation compared to the cw case, which further demonstrates that the pulsed irradiation is more favorable for G-center formation. As an example, even when both beams have an equivalent 10^{13} cm^{-2} proton fluence, the transient PL intensity of G centers formed by the pulsed irradiation is 6 times higher than the PL intensity of the cw-irradiation-induced G centers. On the other hand, a slightly shorter decay time (7 ns) under pulsed irradiation, compared to that of 8.5 ns under

cw at 10^{13} cm^{-2} proton fluence, indicates that the pulse irradiation also introduces more nonradiative defects. Such a dose-rate effect on G-center formation can be related to the protons generating enhanced transient excitations in the silicon, followed by the dynamical annealing by the instantaneous energy deposition. Such transient excitations by pulsed protons affect the mobility of interstitials and/or vacancies, vary the formation energy due to the transient Fermi level, and modulate the rate of G-center creation versus destruction, as well as the rate of vacancy or interstitial accumulation versus annealing within the nanosecond range [41]. In addition, our recent theoretical study indicates that optically active G centers can be altered into an optically inactive configuration by overcoming a conversion barrier of about 0.15 eV [42]. Such a perturbation of G centers formed by previous protons can be triggered by the incoming protons under the cw irradiation.

C. Impact of dose-rate effect on G-center line-width broadening

The optical spectral line width of color centers characterizes the local inhomogeneities, which are usually the dominating factor causing dephasing of a color-center qubit and are an important metric for spin-photon interface applications. As shown in Fig. 3(a), one shot (gray) of $7.9 \pm 1.6 \times 10^{10}$ protons per cm^2 per pulse allows the generation of G centers with narrow line widths < 0.08 nm, whereas the spectrum becomes significantly broadened to 0.13 nm by 100 shots of proton pulses (black). In particular, compared to the single Lorentzian-shape spectrum of one shot of proton pulse, the spectral broadening induced by 100 shots is comprised of two groups of G-center emission with a ± 0.05 nm shift, which likely results from the local strain variation caused by the accumulation of interstitial and/or vacancy clusters. These subtle optical features are consistent with the high-flux-induced heat-spike phenomenon, which leads to a superlinear damage accumulation that creates an underdense region of vacancies in the hot cascade core and an overdense region of Si interstitials pushed outward to the periphery of the cascade core [2,20,43]. On the other hand, with a similar fluence to the 100-shot case, G centers formed by 10^{13} cm^{-2} cw irradiation preserve their narrow line width < 0.08 nm [blue in Fig. 3(a)], which is as narrow as the spectrum produced by the one-shot pulse. This indicates that at low flux levels and for light ions, the radiation-induced interstitials and vacancies mainly recombine before damage overlap occurs. It is indeed reported that the lattice strain associated with the production of a Frenkel pair can induce spontaneous recombination of the vacancy and self-interstitial if they are located within several lattice periods of each other [20,43], which consequently reduces the local strain variation and suppresses the line-width broadening of the G center.

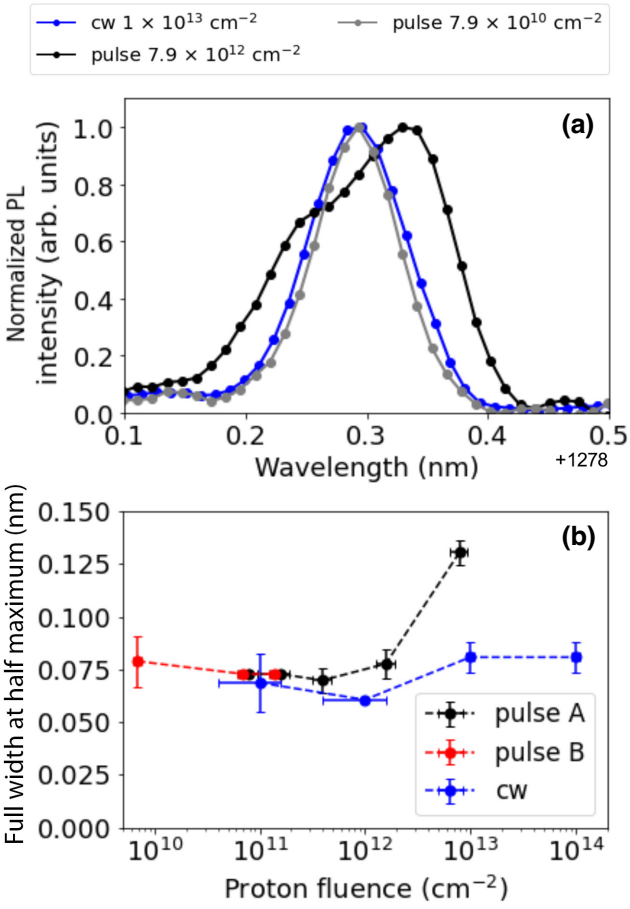

FIG. 3. (a) A comparison of a normalized zero-phonon-line spectrum of G centers generated by 100 shots (black) and one shot (gray) of $7.9 \pm 1.6 \times 10^{10}$ protons per cm^2 per pulse and cw 1×10^{13} protons per cm^2. (b) A comparison of the proton-fluence-dependent line width (full width at half maximum) of G centers generated by irradiation with $7.9 \pm 1.6 \times 10^{10}$ protons per cm^2 per pulse, $6.9 \pm 1.6 \times 10^{9}$ protons per cm^2 per pulse, and cw protons.

Figure 3(b) summarizes the variation of the G-center line width under cw irradiation, which remains < 0.08 nm as the proton fluence increases from 10^{11} cm^{-2} to 10^{14} cm^{-2}. Such a narrow line width is resilient to environmental charge fluctuations within an optical-pump-power range, as shown in Sec. II of the Supplemental Material [36]. The unchanged line width versus the trend toward a shortened PL lifetime as a function of the cw proton fluence suggests that the impact of nonradiative defects on the line widths and decay times of G centers happens at different spatial scales. In detail, only the nonradiative defects that cause the strain-field fluctuation within the spread of the localized state of the G centers contribute to the line-width broadening. The spread of localized-defect states in silicon is typically about a few nanometers [32,42,44]. On the other hand, any nonradiative defects with a distance to G centers within the carrier diffusion length (micrometer

scale [45]) will affect the G-center PL decay and quantum efficiency. Consequently, the PL decay time is more sensitive than the line width to the presence of nonradiative defects. Meanwhile, for the pulsed condition, the transition of line-width broadening from 0.08 nm to 0.13 nm occurs at a fluence of around 10^{12} cm^{-2} (which is nevertheless still narrower than the line width of G centers formed by carbon and proton coimplantation with annealing [33,34]). The PL decay of G centers formed by 100 proton pulses is faster than that of G centers formed by the 10^{13} cm^{-2} cw irradiation, indicating that more vacancy-related nonradiative defects are being introduced by the higher dose rate. This is in line with the onset of clustering of vacancies causing a stronger degree of atomic disorder. In addition, we performed 70-keV Ar irradiation with 10^{12} cm^{-2} fluence on the same Si wafer, which generates damage events at a rate 3 orders of magnitude higher than 1-MeV protons with 10^{13} cm^{-2} fluence. We observed G centers with a broader line width (0.16 nm) formed by the Ar irradiation, which further suggests the formation of vacancy clusters induced by dense damage cascades. From the application aspect, our results demonstrate that the optical signal from (single) G centers enables atomic scale sensing of radiation damage resulting from ultradilute low-fluence irradiation, e.g., expanding capabilities for dark-matter searches [46].

IV. *AB INITIO* MODELING OF INHOMOGENEOUS BROADENING

To understand the origin of inhomogeneous broadening in the G-center spectrum in the presence of radiation damage, first-principles electronic structure calculations of the zero-phonon line (ZPL) were performed using VASP [47–50] with HSE06 hybrid functionals [51,52]. More details of the approach can be found in Sec. III of the Supplemental Material [36]. The radiation damage to the silicon unit cell hosting the G center was simulated by introducing vacancies at lattice sites or silicon interstitials ($Si_{(i)}$) at tetrahedral voids within the structure, in order to modify the G center. The G center in silicon has two possible structural configurations, of which the type-B configuration is optically active and is composed of two substitutional carbon atoms, with a silicon self-interstitial in between. For the type-B configuration (as shown in Sec. III of the Supplemental Material [36]) of the G center (GCB) embedded into a $3 \times 3 \times 3$ silicon supercell, there are 215 possible silicon sites that can be replaced by vacancies, including the $Si_{(i)}$ that is part of the G center itself [42,53], as well as 106 tetrahedral voids into which an additional $Si_{(i)}$ can be introduced. It has previously been established that self-interstitials and vacancies in silicon can exist in various charge states depending on the position of the Fermi level, ranging from -2 to $+2$ for $Si_{(i)}$ [54] and 0, $+1$, and $+2$ for vacancies [55]. For our configuration, we computed formation energies [56] by setting the chemical potential at the valence-band maximum, to establish the $+2$ as the most stable charge state for both defects, consistent with prior studies. We note that the dimension of the silicon supercell $(1.63\ \text{nm})^3$ and periodic boundary conditions limit the maximum separation between the GCB and the defect to about approximately 1 nm, which is considerably less than the average separation generated in experiments. Nevertheless, the modeling provides a qualitative understanding of the broadening and shape of the emission spectrum. In addition, we note that some of these configurations have been excluded from the plot, because of nonconvergence within the density functional theory self-consistent cycle as a result of the close proximity of the GCB and the interstitial or vacancy.

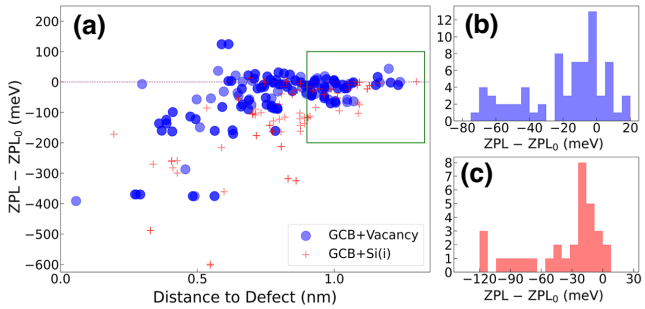

FIG. 4. (a) The shift of the ZPL transition energy versus the distance between the GCB and the perturbing defect, where the defect is a vacancy (blue circles) or a silicon self-interstitial (red cross). (b),(c) Histograms of the ZPL shift due to (b) vacancies and (c) self-interstitials for the region marked by the green box in (a).

For these 321 modified G-center structures, force-relaxed ground- and excited-state structures were computed to obtain the ZPL transition energies versus the distance to defects, shown in Fig. 4(a). Similarly, the shifts of singlet-triplet transition of the G center by defects are presented in Sec. IV of the Supplemental Material [36]. The distribution of ZPLs is broadened dramatically along with a collective red shift when the defects are closer than 0.5 nm to the G center. The behavior of configurations where the defects are farthest (approximately 1 nm) from the GCB has previously been identified as relatively closely representative of experiments [32]. For separations > 0.9 nm, the distribution of ZPLs is considerably narrower and we plot histograms of the ZPL shifts for vacancies and $Si_{(i)}$ in Figs. 4(b) and 4(c), respectively. These show that vacancies appear to generate bilateral red and blue shifts in the ZPL, while the $Si_{(i)}$ have a tendency toward red shift. As summarized in Sec. V of the Supplemental Material [36], we further extrapolate that the 0.1-nm (100-μeV) broadening of the ZPL of a G center can be attributed to the presence of a vacancy (or self-interstitial) at a distance of a few nanometers.

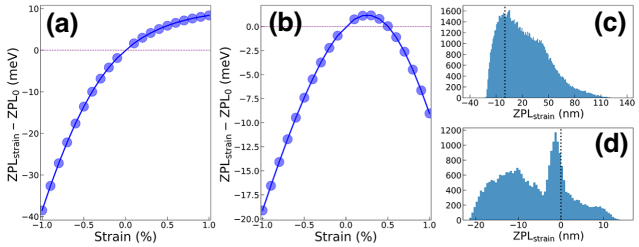

FIG. 5. (a),(b) The ZPL shift versus the strain for the (a) x and (b) z directions. (c),(d) The distribution of combined ZPL shifts for (c) a uniform selection of $< x, y, z >$ strain vectors and (d) a distribution biased in the $< 001 >$ direction.

The effect of the local defects on the ZPL of the GCB can be understood in terms of the local strain that they induce. To isolate the impact of local strain, we perform strain calculations on an isolated G center ranging from -1% to $+1\%$ in increments of 0.1% for x, y, and z linear strains, x-y, x-z, and y-z in-plane strains, and isotropic xyz strain as detailed in Sec. VI of the Supplemental Material [36]. In addition, due to the $< 110 >$ mirror-plane symmetry of the G center, strains along the x and y directions will be equivalent, and strains along the x-z and y-z planes will be equivalent as well. The ZPL shifts due to strain in the x and z directions are shown in Figs. 5(a) and 5(b) and can be used to interpret the effect of vacancies and silicon self-interstitials on the G-center emission. In particular, a vacancy will result in nearby silicon atoms relaxing to fill the void and will lead to a tensile strain that expands the lattice around any nearby G centers, as has been proposed previously [12]. This tensile strain can result in either a red shift or blue shift of the ZPL, depending on the relative position of the vacancy and the GCB, explaining the bimodal distribution seen in Fig. 4(b). Conversely, $Si_{(i)}$ would lead to compressive strain on the GCB, which always results in a red shift [Fig. 4(c)], regardless of the defect position.

More detailed modulation of the distribution of ZPL shifts occurs when we further consider a distribution of defect locations (strains). As an example, we select a uniform distribution of 10^5 strain vectors with random x, y, and z components ranging from -1% to $+1\%$ and interpolate the effect on the ZPL by adding the shift generated by each strain direction. The resulting ZPL distribution is shown in Fig. 5(c) and is consistent with the histogram plots in Figs. 4(b) and 4(c), showing the characteristic red-shifted shoulder. For this distribution of strains, the resulting ZPL distribution may be explained by x-directional strains favoring large red shifts and z-directional strains causing comparatively smaller ZPL shifts. We also note that the proton irradiation will not necessarily result in a uniform distribution of vacancies and interstitials around the G centers. This distribution of ZPL shifts is highly dependent on the distribution of strains. In Fig. 5(d), we compute the distribution of combined ZPL shifts for a sample of $< x, y, z >$ strain vectors heavily biased in the z direction, using the procedure described in Sec. III of the Supplemental Material [36]. The ZPL shifts generated in this way create the spectrum with a broad blue-shifted component and a relatively concentrated component near the original ZPL, which is qualitatively similar to our previous experimental spectrum obtained in the high-damage limit [32], where such a biased distribution of local strains might be expected. In principle, such a procedure can be inverted to estimate possible local strain distributions from measured spectra and in turn determine the distribution of defect damage near silicon G centers.

While these first-principles calculations were performed for small GCB-defect separations, their interpretation in terms of strain fields allows us to understand the behavior at larger GCB-defect separations present in our samples. A possible explanation for the two peaks in the experimental PL spectra [Fig. 3(a)] is the presence of two separate populations of defect-induced strain: one arising from interstitials resulting in red shifts and one from vacancies, resulting in blue or red shifts clustered around different mean values. Based on our predictions of the ZPL-strain relation, we estimate the experimental local strains around the G centers to be of the order of 0.01%. Therefore, the collective strain introduced by adding vacancies and interstitials near a G center qualitatively explains the experimentally observed spectral broadening and dominant red shift of the G-center spectrum caused by high-flux and high-fluence pulsed-proton irradiation.

V. CONCLUSIONS

In conclusion, we have studied the formation dynamics of G color centers in silicon far from equilibrium under various dose rates of proton beams. Compared to cw proton irradiation, pulse excitation offers the benefit of enhanced transient excitations and lattice heating by the instantaneous energy deposition in about 10-ns-long proton pulses, which allows optimization of the ratio of G-center formation to destruction and to nonradiative defect accumulation within the nanosecond time regime. By characterizing the PL of G centers, our results highlight the approach of pulsed-proton irradiation on silicon wafers to generate color-center complexes with high formation efficiency while preserving narrow line widths. Our results can inform the optimization of (single) G-center formation by pulsed-ion implantation and exploration of pulsed-ion beams for the synthesis of other quantum defects. Moreover, compared to the broadening of G-center ensemble line widths by residual lattice damage from carbon-ion implantation and thermal annealing, the narrow line widths of G centers created by our approach allows them to be used as a sensitive probe of atomic radiation damage when the irradiation condition is above a certain threshold of

dense damage cascades. The PL of G centers is a readily available analytical method for radiation-damage studies [7]. Aided by *ab initio* electronic structure calculations, we have provided insight into the atomic disorder induced inhomogeneous broadening by introducing vacancies and Si interstitials in the vicinity of a G center. A vacancy leading to a tensile strain can result in either a red shift or a blue shift of the G-center emission, depending on its position relative to the G center. Meanwhile, Si interstitials lead to compressive strain, which results in a monotonic red shift. The calculation also reveals that the G-center ZPL distribution can be modulated by the strain fields oriented in specific directions. The intense and tunable proton and ion pulses (from induction accelerators or laser acceleration) enable studies of fundamental defect dynamics of radiation-induced defects, defect engineering, and qubit synthesis for quantum information processing.

The data that support the results of this study are available from the corresponding author upon reasonable request.

ACKNOWLEDGMENTS

Work at Lawrence Berkeley National Laboratory was supported by the Office of Science, Office of Fusion Energy Sciences, of the U.S. Department of Energy, by the program on Quantum Information Science Enabled Discovery (QuantISED) for High Energy Physics, and by the Molecular Foundry, a DOE Office of Science User Facility supported by the Office of Science of the U.S. Department of Energy under Contract No. DE-AC02-05CH11231. This research used resources of the National Energy Research Scientific Computing Center, a DOE Office of Science User Facility supported by the Office of Science of the U.S. Department of Energy under Contract No. DE-AC02-05CH11231.

The proton irradiation and sample preparation were performed by W.L., Q.J., A.P., K.J., T.S. and J.G.L. The PL measurements were performed by W.L., W.R. and Y.Z. All the theoretical calculations were performed by V.I. with support from J.S. and L.Z.T. The manuscript was written by W.L. and V.I. and edited by all authors. T.S., L.Z.T. and B.K. supervised the project.

The authors declare no competing financial or nonfinancial interests.

[1] G. Moody, *et al.*, 2022 roadmap on integrated quantum photonics, J. Phys.: Photon. **4**, 012501 (2022).

[2] M. Gimeno-Segovia, T. Rudolph, and S. E. Economou, Deterministic Generation of Large-Scale Entangled Photonic Cluster State from Interacting Solid State Emitters, Phys. Rev. Lett. **123**, 070501 (2019).

[3] W. Gao, P. Fallahi, E. Togan, J. Miguel-Sánchez, and A. Imamoglu, Observation of entanglement between a quantum dot spin and a single photon, Nature **491**, 426 (2012).

[4] J. Wang, S. Paesani, Y. Ding, R. Santagati, P. Skrzypczyk, A. Salavrakos, J. Tura, R. Augusiak, L. Mančinska, D. Bacco, D. Bonneau, J. W. Silverstone, Q. Gong, A. Acín, K. Rottwitt, L. K. Oxenløwe, J. L. O'Brien, A. Laing, and M. G. Thompson, Multidimensional quantum entanglement with large-scale integrated optics, Science **360**, 285 (2018).

[5] J. Wang, F. Sciarrino, A. Laing, and M. G. Thompson, Integrated photonic quantum technologies, Nat. Photon. **14**, 273 (2020).

[6] S. Fathpour, Emerging heterogeneous integrated photonic platforms on silicon, Nanophotonics **4**, 143 (2015).

[7] G. Davies, The optical properties of luminescence centres in silicon, Phys. Rep. **176**, 83 (1989).

[8] D. B. Higginbottom, *et al.*, Optical observation of single spins in silicon, Nature **607**, 266 (2022).

[9] W. Redjem, A. Durand, T. Herzig, A. Benali, S. Pezzagna, J. Meijer, A. Y. Kuznetsov, H. S. Nguyen, S. Cueff, J. M. Gérard, I. Robert-Philip, B. Gil, D. Caliste, P. Pochet, M. Abbarchi, V. Jacques, A. Dréau, and G. Cassabois, Single artificial atoms in silicon emitting at telecom wavelengths, Nat. Electron. **3**, 738 (2020).

[10] T. Schenkel, W. Redjem, A. Persaud, W. Liu, P. A. Seidl, A. J. Amsellem, B. Kanté, and Q. Ji, Exploration of defect dynamics and color center qubit synthesis with pulsed ion beams, Quantum Beam Sci. **6**, 13 (2022).

[11] L. Komza, P. Samutpraphoot, M. Odeh, Y.-L. Tang, M. Mathew, J. Chang, H. Song, M.-K. Kim, Y. Xiong, G. Hautier, and A. Sipahigil, Indistinguishable photons from an artificial atom in silicon photonics (2022), arXiv preprint ArXiv:2211.09305.

[12] W. Redjem, Y. Zhiyenbayev, W. Qarony, V. Ivanov, C. Papapanos, W. Liu, K. Jhuria, Z. Y. Al Balushi, S. Dhuey, A. Schwartzberg, L. Z. Tan, T. Schenkel, and B. Kanté, All-silicon quantum light source by embedding an atomic emissive center in a nanophotonic cavity, Nat. Commun. **14**, 3321 (2023).

[13] D. Dhaliah, Y. Xiong, A. Sipahigil, S. M. Griffin, and G. Hautier, First-principles study of the T center in silicon, Phys. Rev. Mater. **6**, L053201 (2022).

[14] A. Gritsch, L. Weiss, J. Früh, S. Rinner, and A. Reiserer, Narrow Optical Transitions in Erbium-Implanted Silicon Waveguides, Phys. Rev. X **12**, 041009 (2022).

[15] C. Yin, M. Rancic, G. G. de Boo, N. Stavrias, J. C. McCallum, M. J. Sellars, and S. Rogge, Optical addressing of an individual erbium ion in silicon, Nature **497**, 91 (2013).

[16] H. Kraner, Radiation damage in semiconductor detectors, IEEE Trans. Nucl. Sci. **29**, 1087 (1982).

[17] M. Moll, Displacement damage in silicon detectors for high energy physics, IEEE Trans. Nucl. Sci. **65**, 1561 (2018).

[18] A. Y. Polyakov, S. Pearton, P. Frenzer, F. Ren, L. Liu, and J. Kim, Radiation effects in GaN materials and devices, J. Mater. Chem. C **1**, 877 (2013).

[19] S. Pearton, A. Haque, A. Khachatrian, A. Ildefonso, L. Chernyak, and F. Ren, Opportunities in single event effects in radiation-exposed SiC and GaN power electronics, ECS J. Solid State Sci. Technol. **10**, 075004 (2021).

[20] K. Nordlund, S. J. Zinkle, A. E. Sand, F. Granberg, R. S. Averback, R. E. Stoller, T. Suzudo, L. Malerba, F. Banhart, W. J. Weber, F. Willaime, S. L. Dudarev, and D. Simeone, Primary radiation damage: A review of current understanding and models, J. Nucl. Mater. **512**, 450 (2018).

[21] J. Wallace, S. Charnvanichborikarn, L. Bayu Aji, M. Myers, L. Shao, and S. Kucheyev, Radiation defect dynamics in Si at room temperature studied by pulsed ion beams, J. Appl. Phys. **118**, 135709 (2015).

[22] A. Hallén, D. Fenyö, B. Sundqvist, R. Johnson, and B. Svensson, The influence of ion flux on defect production in MeV proton-irradiated silicon, J. Appl. Phys. **70**, 3025 (1991).

[23] P. Leveque, A. Hallén, P. Pellegrino, B. Svensson, and V. Privitera, Dose-rate influence on the defect production in MeV proton-implanted float-zone and epitaxial n-type silicon, Nucl. Instrum. Methods Phys. Res. Sect. B: Beam Interact. Mater. At. **186**, 375 (2002).

[24] K. Borer, *et al.*, Charge collection efficiency of irradiated silicon detector operated at cryogenic temperatures, Nucl. Instrum. Methods Phys. Res. Sect. A: Accelerators, Spectrometers, Detectors and Associated Equip. **440**, 5 (2000).

[25] A. Titov and G. Carter, Defect accumulation during room temperature N^+ irradiation of silicon, Nucl. Instrum. Methods Phys. Res. Sect. B: Beam Interact. Mater. At. **119**, 491 (1996).

[26] J. Wallace, L. B. Aji, L. Shao, and S. Kucheyev, Deterministic Role of Collision Cascade Density in Radiation Defect Dynamics in Si, Phys. Rev. Lett. **120**, 216101 (2018).

[27] H. Minagawa, N. Shunsuke, M. Masaki, K. Atsuo, and T. Hidetsugu, in *JJAP Conference Proceedings*, Vol. 7 (The Japan Society of Applied Physics, 2017).

[28] M. Hollenbach, N. Klingner, N. S. Jagtap, L. Bischoff, C. Fowley, U. Kentsch, G. Hlawacek, A. Erbe, N. V. Abrosimov, M. Helm, Y. Berencén, and G. V. Astakhov, Wafer-scale nanofabrication of telecom single-photon emitters in silicon, Nat. Commun. **13**, 7683 (2022).

[29] H. Quard, M. Khoury, A. Wang, T. Herzig, J. Meijer, S. Pezzagna, S. Cueff, D. Grojo, M. Abbarchi, H. S. Nguyen, N. Chauvin, and T. Wood, Femtosecond laser induced creation of G and W-centers in silicon-on-insulator substrates (2023), arXiv preprint ArXiv:2304.03551.

[30] T. Schenkel, S. Lidia, C. Weis, W. Waldron, J. Schwartz, A. M. Minor, P. Hosemann, and J. Kwan, Towards pump-probe experiments of defect dynamics with short ion beam pulses, Nucl. Instrum. Methods Phys. Res. Sect. B: Beam Interact. Mater. At. **315**, 350 (2013).

[31] J. G. López, F. Ager, M. B. Rank, F. Madrigal, M. Ontalba, M. Respaldiza, and M. Ynsa, CNA: The first accelerator-based IBA facility in Spain, Nucl. Instrum. Methods Phys. Res. Sect. B: Beam Interact. Mater. At. **161**, 1137 (2000).

[32] W. Redjem, *et al.*, Defect engineering of silicon with ion pulses from laser acceleration, Commun. Mater. **4**, 22 (2023).

[33] C. Beaufils, W. Redjem, E. Rousseau, V. Jacques, A. Y. Kuznetsov, C. Raynaud, C. Voisin, A. Benali, T. Herzig, S. Pezzagna, J. Meijer, M. Abbarchi, and G. Cassabois, Optical properties of an ensemble of G-centers in silicon, Phys. Rev. B **97**, 035303 (2018).

[34] D. D. Berhanuddin, M. A. Lourenço, R. M. Gwilliam, and K. P. Homewood, Co-implantation of carbon and protons: An integrated silicon device technology compatible method to generate the lasing G-center, Adv. Funct. Mater. **22**, 2709 (2012).

[35] F. Treffert, Q. Ji, P. A. Seidl, A. Persaud, B. Ludewigt, J. J. Barnard, A. Friedman, D. P. Grote, E. P. Gilson, I. D. Kaganovich, A. Stepanov, M. Roth, and T. Schenkel, Design and implementation of a Thomson parabola for fluence dependent energy-loss measurements at the neutralized drift compression experiment, Rev. Sci. Instrum. **89**, 103302 (2018).

[36] See sections I) to VI) in the Supplemental Material at http://link.aps.org/supplemental/10.1103/PhysRevApplied.20.014058 for (I) the basics of carrier-recombination dynamics and time-resolved photoluminescence; (II) the pump-power-dependent optical properties; (III) details of first-principles calculations and modeling of the ZPL distribution with strain vectors biased in the z direction; (IV) the dependence of the G center triplet transition on disorder; (V) the effect of vacancies and interstitials at relatively large distances from a G center on G center ZPL, and (VI) more details on the strain calculations. The Supplemental Material also contains Refs. [57,58].

[37] M. Huhtinen, Simulation of non-ionising energy loss and defect formation in silicon, Nucl. Instrum. Methods Phys. Res. Sect. A: Accelerators, Spectrometers, Detectors and Associated Equip. **491**, 194 (2002).

[38] W. B. Jackson and N. M. Amer, Direct measurement of gap-state absorption in hydrogenated amorphous silicon by photothermal deflection spectroscopy, Phys. Rev. B **25**, 5559 (1982).

[39] W. Liu, J.-F. Carlin, N. Grandjean, B. Deveaud, and G. Jacopin, Exciton dynamics at a single dislocation in GaN probed by picosecond time-resolved cathodoluminescence, Appl. Phys. Lett. **109**, 042101 (2016).

[40] G. Rossbach, J. Levrat, G. Jacopin, M. Shahmohammadi, J.-F. Carlin, J.-D. Ganière, R. Butté, B. Deveaud, and N. Grandjean, High-temperature Mott transition in wide-band-gap semiconductor quantum wells, Phys. Rev. B **90**, 201308 (2014).

[41] J. Wallace, L. Aji, A. Martin, S. Shin, L. Shao, and S. Kucheyev, The role of Frenkel defect diffusion in dynamic annealing in ion-irradiated Si, Sci. Rep. **7**, 1 (2017).

[42] V. Ivanov, J. Simoni, Y. Lee, W. Liu, K. Jhuria, W. Redjem, Y. Zhiyenbayev, C. Papapanos, W. Qarony, B. Kanté, A. Persaud, T. Schenkel, and L. Z. Tan, Effect of localization on photoluminescence and zero-field splitting of silicon color centers, Phys. Rev. B **106**, 134107 (2022).

[43] H. Niu, J. Zhao, H. Li, Y. Sun, J. H. Park, Y. Jing, W. Li, J. Yang, and X. Li, A machine-learning interatomic potential to understand primary radiation damage of silicon, Comput. Mater. Sci. **218**, 111970 (2023).

[44] J. Smith, A. Budi, M. Per, N. Vogt, D. Drumm, L. Hollenberg, J. Cole, and S. Russo, *Ab initio* calculation of energy levels for phosphorus donors in silicon, Sci. Rep. **7**, 1 (2017).

[45] L. C. Andreani, A. Bozzola, P. Kowalczewski, M. Liscidini, and L. Redorici, Silicon solar cells: Toward the efficiency limits, Adv. Phys.: X **4**, 1548305 (2019).

[46] R. Ebadi, M. C. Marshall, D. F. Phillips, J. Cremer, T. Zhou, M. Titze, P. Kehayias, M. Saleh Ziabari, N. Delegan, S. Rajendran, A. O. Sushkov, F. J. Heremans, E.

S. Bielejec, M. V. Holt, and R. L. Walsworth, Directional detection of dark matter using solid-state quantum sensing, AVS Quantum Sci. **4**, 044701 (2022).

[47] G. Kresse and J. Hafner, *Ab initio* molecular dynamics for liquid metals, Phys. Rev. B **47**, 558 (1993).

[48] G. Kresse and J. Hafner, *Ab initio* molecular-dynamics simulation of the liquid-metal–amorphous-semiconductor transition in germanium, Phys. Rev. B **49**, 14251 (1994).

[49] G. Kresse and J. Furthmüller, Efficiency of *ab-initio* total energy calculations for metals and semiconductors using a plane-wave basis set, Comput. Mater. Sci. **6**, 15 (1996).

[50] G. Kresse and J. Furthmüller, Efficient iterative schemes for *ab initio* total-energy calculations using a plane-wave basis set, Phys. Rev. B **54**, 11169 (1996).

[51] A. V. Krukau, O. A. Vydrov, A. F. Izmaylov, and G. E. Scuseria, Influence of the exchange screening parameter on the performance of screened hybrid functionals, J. Chem. Phys. **125**, 224106 (2006).

[52] H. Wang, A. Chroneos, C. A. Londos, E. N. Sgourou, and U. Schwingenschlögl, G-centers in irradiated silicon revisited: A screened hybrid density functional theory approach, J. Appl. Phys. **115**, 183509 (2014).

[53] L. W. Song, X. D. Zhan, B. W. Benson, and G. D. Watkins, Bistable interstitial-carbon–substitutional-carbon pair in silicon, Phys. Rev. B **42**, 5765 (1990).

[54] J. A. Stewart, N. A. Modine, and R. Dingreville, Re-examining the silicon self-interstitial charge states and defect levels: A density functional theory and bounds analysis study, AIP Adv. **10**, 095004 (2020).

[55] Y. Yamakawa and Y. Ōno, Cluster model calculations for charge states of a silicon vacancy, J. Phys.: Conf. Ser. **150**, 042233 (2009).

[56] M. Arrigoni and G. K. Madsen, SPINNEY: Post-processing of first-principles calculations of point defects in semiconductors with PYTHON, Comput. Phys. Commun. **264**, 107946 (2021).

[57] C. Chartrand, L. Bergeron, K. Morse, H. Riemann, N. Abrosimov, P. Becker, H.-J. Pohl, S. Simmons, and M. Thewalt, Highly enriched ^{28}Si reveals remarkable optical linewidths and fine structure for well-known damage centers, Phys. Rev. B **98**, 195201 (2018).

[58] P. Udvarhelyi, B. Somogyi, G. Thiering, and A. Gali, Identification of a Telecom Wavelength Single Photon Emitter in Silicon, Phys. Rev. Lett. **127**, 196402 (2021).